The Astronomical Journal, 168:145 (9pp), 2024 October https://doi.org/10.3847/1538-3881/ad6b7f
© 2024. The Author(s). Published by the American Astronomical Society.
OPEN ACCESS

SOLES XII. The Aligned Orbit of TOI-2533 b, a Transiting Brown Dwarf Orbiting an F8-type Star

Thiago Ferreira dos Santos[1], Malena Rice[1], Xian-Yu Wang[2], and Songhu Wang[2]
[1] Department of Astronomy, Yale University, 219 Prospect Street, New Haven, CT 06511, USA; thiago.dossantos@yale.edu
[2] Department of Astronomy, Indiana University, 727 East 3rd Street, Bloomington, IN 47405-7105, USA
Received 2024 May 23; revised 2024 July 30; accepted 2024 August 2; published 2024 September 5

Abstract

Brown dwarfs occupy a middle ground in mass space between gaseous giant planets and ultracool dwarf stars, and the characterisation of their orbital orientations may shed light on how these neighbouring objects form. We present an analysis of the Rossiter–McLaughlin effect across the transit of TOI-2533 *b*, a brown dwarf on a moderately eccentric ($e_b = 0.2476 \pm 0.0090$) and wide-separation ($a_b/R_\star = 13.34 \pm 0.30$) orbit around an F8-type star, using data from the NEID/WIYN spectrograph in combination with archival photometry and radial velocity observations. Spin-orbit analyses of brown dwarfs are relatively rare, and TOI-2533 stands out as the fifth brown dwarf system with a measured spin–orbit constraint. We derive a sky-projected stellar obliquity of $\lambda = -7^\circ \pm 14^\circ$ for TOI-2533 *b*, finding that the brown dwarf is consistent with spin–orbit alignment. Our joint model also indicates that TOI-2533 *b* falls near the lower bound of the hydrogen-burning minimum mass range ($M_b = 74.9 \pm 5.3\, M_{\rm Jup}$). Ultimately, we find that TOI-2533 *b* is consistent with formation from disc fragmentation in a primordially spin–orbit aligned orientation, although we cannot rule out the possibility that the system has been tidally realigned during its lifetime.

Unified Astronomy Thesaurus concepts: Brown dwarfs (185); Exoplanet dynamics (490); Exoplanet formation (492); Exoplanet evolution (491); Planetary alignment (1243); Star-planet interactions (2177); Binary stars (154); Close binary stars (254)

1. Introduction

The formation of eclipsing systems—including exoplanets, brown dwarfs, and stars—can be constrained at a population level, and in some cases at an individual-system level, through precise measurements of the masses and relative orbits of the system components (e.g., Winn et al. 2009, 2010; Schlaufman 2010; Albrecht et al. 2012, 2013; Rice et al. 2022b, 2024). The key formation channels of brown dwarfs, whether star-like or planet-like (or a mix), have been long contested (e.g., Bate et al. 2002; Goodwin & Whitworth 2007; Bonnell et al. 2008; Maldonado & Villaver 2017; Bowler et al. 2020). While a rough mass cutoff is generally used for convenience to delineate the borders between planets ($M \lesssim 13 M_{\rm Jup}$), brown dwarfs ($M \sim 13$–$80 M_{\rm Jup}$), and stars ($M \gtrsim 80 M_{\rm Jup}$), an improved understanding of the formation mechanisms that separate each regime, including what properties typically characterize each group, is needed to define physically motivated boundaries (e.g., Schlaufman 2018).

Divergent eccentricity distributions for substellar companions suggest distinct formation mechanisms at the high- and low-mass end. For example, Ma & Ge (2014) showed that systems with low-mass ($M_{\rm BD} < 42.5\, M_{\rm Jup}$) brown-dwarf companions demonstrate an anticorrelation between mass and maximum eccentricity, whereas this trend is not apparent for systems with high-mass brown-dwarf companions ($M_{\rm BD} > 42.5\, M_{\rm Jup}$), which follow an eccentricity distribution more similar to that of stellar binaries. Bowler et al. (2020) more recently showed that high-mass-ratio systems ($M_{\rm BD}/M_* > 0.01$) follow a broader eccentricity distribution than low-mass-ratio systems ($M_{\rm BD}/M_* < 0.01$), which tend toward lower eccentricities. These findings suggest that low-mass ($M_{\rm BD} < 42.5\, M_{\rm Jup}$) and low-mass-ratio ($q < 0.01$) brown-dwarf companions may form through gravitational instability within circumstellar disks (Boss 1997), while high-mass ($M_{\rm BD} > 42.5\, M_{\rm Jup}$) and high-mass-ratio ($M_{\rm BD}/M_* > 0.01$) brown-dwarf companions instead form more like stars, through molecular cloud collapse (Larson 1969; Tohline 2002).

Improved characterization of brown-dwarf systems, particularly in light of a growing population of known transiting brown dwarfs (Šubjak et al. 2020; Carmichael et al. 2021, 2022; Psaridi et al. 2022; Carmichael 2023) with the advent of the Transiting Exoplanet Survey Satellite (TESS; Ricker et al. 2015), offers a compelling path forward to further distinguish between planet-like and star-like formation histories. Each formation mechanism should have a distinct imprint on the final distribution of brown-dwarf spin–orbit orientations—that is, the alignment of the brown dwarf's orbit normal with the spin axis of its host star. Turbulent fragmentation, for instance, may result in a diverse range of orientations (Offner et al. 2016), while disk-based pathways are typically linked to primordial alignment (although see Bate et al. 2003, 2010 for exceptions).

Spin–orbit orientations can be observationally constrained for transiting systems (see Albrecht et al. 2022 for a review of this topic). During the transit of a spin–orbit aligned occulter, the blueshifted hemisphere of a star is first obscured, followed by an equal-duration obscuration of the redshifted hemisphere (Holt 1893). The corresponding distortion in the net Doppler shift measured across the integrated light from the star during the transit event is known as the Rossiter–McLaughlin (RM) effect (McLaughlin 1924; Rossiter 1924).

Original content from this work may be used under the terms of the Creative Commons Attribution 4.0 licence. Any further distribution of this work must maintain attribution to the author(s) and the title of the work, journal citation and DOI.

The RM effect can be measured to derive the sky-projected spin–orbit angle λ (a 2D proxy for the true, 3D spin–orbit angle ψ) between the stellar spin axis and the occulter's orbit normal. Asymmetries in the RM profile are indicative of orbits that are misaligned with the host star's equator, hinting that a particular system either did not emerge from a spin–orbit aligned circumstellar disk or that it was dynamically perturbed after disk dispersal (e.g., Naoz et al. 2011, 2012; Teyssandier et al. 2019).

To date,[3] orbital obliquity measurements have been reported for 211 transiting exoplanets and brown dwarfs, with most of the observations focused on short-period, Jovian-mass exoplanet companions. Among these systems, only four RM observations have been reported for transiting brown dwarfs: CoRoT-3b ($\lambda = -37.6^{+10.0}_{-22.3}$ deg, $M = 21.23^{+0.82}_{-0.59}\,M_{\rm Jup}$; Triaud et al. 2009), KELT-1b ($\lambda = 2 \pm 16$ deg, $M = 27.38 \pm 0.93\,M_{\rm Jup}$; Siverd et al. 2012), WASP-30b ($\lambda = 7^{+19}_{-27}$ deg, $M = 62.5 \pm 1.2\,M_{\rm Jup}$; Triaud et al. 2013), and HATS-70b ($\lambda = 8.9^{+5.6}_{-4.5}$ deg, $M = 12.9^{+1.8}_{-1.6}\,M_{\rm Jup}$; Zhou et al. 2019). Brown-dwarf spin–orbit observations remain rare, despite their utility to constrain the formation pathways of these systems.

In this paper, we present an RM analysis of TOI-2533 *b*, a brown dwarf with orbital period $P \sim 6.68$ days first confirmed by Schmidt et al. (2023) that transits an F8-type star bordering the Kraft break (Kraft 1967). Our study leverages observations obtained using the NEID Spectrograph (Schwab et al. 2016) on the WIYN 3.5 m Telescope. This is the twelfth result in the Stellar Obliquities in Long-period Exoplanet Systems (SOLES) survey (Rice et al. 2021, 2022b, 2023a, 2023b; Wang et al. 2022; Dong et al. 2023; Hixenbaugh et al. 2023; Lubin et al. 2023; Wright et al. 2023; Hu et al. 2024; Radzom et al. 2024), which is designed to extend the set of spin–orbit constraints to relatively wide-orbiting substellar companions. The observations of TOI-2533 obtained within this work are described in Section 2, and a description of the stellar fundamental parameters are presented in Section 3. The joint transit, radial velocity, and RM effect models are presented in Section 4, and we discuss dynamical timescales in Section 5. Insights into the formation and evolution of TOI-2533 *b* and its placement among other transiting brown dwarfs with measured spin–orbit orientations are presented in Section 6. Our conclusions are then given in Section 7.

2. Observations

We obtained 21 in-transit radial velocity measurements of TOI-2533 (TYC 2010-124-1; Gaia DR3 1259922196651254272; TIC 418012030) in high-resolution mode ($R \sim 110{,}000$) with the NEID Spectrograph mounted on the 3.5 m WIYN Telescope at Kitt Peak National Observatory in Arizona/US (Schwab et al. 2016). Observations were performed on 2023 April 15, from 06:37 to 11:42 UT, with exposure times of 900 s resulting in an average SNR $= 20.8\,{\rm px}^{-1}$ at 5500 Å. Air masses varied from 1.06 at the beginning of the observations to 1.47 at the end, and the collected radial velocities are provided in Table 1. The data was reduced using the NEID Data Reduction Pipeline (Kaplan et al. 2019).

[3] As of 2024 May; based on the Encyclopaedia of Exoplanetary Systems (https://exoplanet.eu/home/) and the Transiting Exoplanets Catalogue (TEPCat; Southworth 2011; https://astro.keele.ac.uk/jkt/tepcat/tepcat.html).

Table 1
In-transit Radial Velocities for the TOI-2533 System Collected with NEID/WIYN Spectrograph

Time (BJD)	RV (km s^{-1})	$\sigma_{\rm RV}$ (km s^{-1})
2460049.7864386	−9.6693	0.0114
2460049.7966859	−9.7940	0.0108
2460049.8075163	−9.9099	0.0116
2460049.8182185	−10.0251	0.0122
2460049.8288248	−10.1373	0.0119
2460049.8397229	−10.2756	0.0114
2460049.8498363	−10.3747	0.0115
2460049.8607308	−10.4801	0.0110
2460049.8713124	−10.5995	0.0106
2460049.8821565	−10.7191	0.0114
2460049.8924628	−10.8390	0.0105
2460049.9031508	−10.9848	0.0101
2460049.9136643	−11.1078	0.0101
2460049.9242635	−11.2587	0.0102
2460049.9347213	−11.3692	0.0108
2460049.9454090	−11.5017	0.0107
2460049.9560650	−11.6314	0.0119
2460049.9666020	−11.7174	0.0129
2460049.9773795	−11.8458	0.0136
2460049.9879091	−11.9614	0.0133
2460049.9987549	−12.0692	0.0138

3. Stellar Characterization

3.1. Atmospheric Parameters

We performed a spectral fitting analysis on our co-added out-of-transit NEID spectra, employing the `iSpec` Python package (Blanco-Cuaresma et al. 2014; Blanco-Cuaresma 2019), to derive stellar atmospheric parameters for TOI-2533. From this fit, we obtained $T_{\rm eff} = 6228 \pm 114$ K, $\log g = 4.45 \pm 0.18$ cm s^{-2}, [Fe/H] $= -0.33 \pm 0.07$, and $v \sin i_* = 5.55 \pm 0.75$ km s^{-1}. Our derived values agree with those from Schmidt et al. (2023) within 2σ.

3.2. SED Analysis

We also leveraged the empirical stellar spectra library of Kesseli et al. (2017) to further characterize the TOI-2533 host star. Our SED fit drew archival data from the Two Micron All Sky Survey (Skrutskie et al. 2006), Gaia DR3 (Gaia Collaboration et al. 2023), the Hubble Space Telescope (Windhorst et al. 2011), the Javalambre Physics of the Accelerating Universe Astrophysical Survey (Benitez et al. 2014), the Javalambre-Photometric Local Universe Survey (Cenarro et al. 2019), the Sloan Digital Sky Survey (York et al. 2000), the Tycho-2 Catalogue (Høg et al. 2000), and the Wide-field Infrared Survey Explorer (Wright et al. 2010).

By integrating the observed spectral energy distribution (SED) from the optical ($\lambda_{\rm min} = 3551.05$ Å) to the infrared region ($\lambda_{\rm max} = 115608$ Å) within the Virtual Observatory SED Analyser (VOSA;[4] Bayo et al. 2008), we found that TOI-2533 is an F8-type star. The mass ($1.10^{+0.01}_{-0.04}\,M_\odot$), radius ($1.12 \pm 0.02\,R_\odot$), and effective temperature (6183^{+16}_{-84} K) derived from the SED fitting also agree with the values reported in Schmidt et al. (2023).

[4] http://svo2.cab.inta-csic.es/theory/vosa/

We note that this analysis was conducted independently of the joint fit described in Section 4. Parameters from Schmidt et al. (2023), obtained through spectroscopic analyses, were adopted as priors to derive the stellar host's physical and orbital parameters.

3.3. Additional System Properties

We searched for signatures of rotational variability within our TESS photometry of the TOI-2533 star using both the generalized Lomb–Scargle periodogram (Zechmeister & Kürster 2009) and an Autocorrelation Function analysis (Huber et al. 2009; Viani et al. 2019). No consistent, statistically significant rotational signal was detected, such that we were unable to derive the degree of line-of-sight alignment or the 3D spin–orbit orientation. We also found no evidence for bound stellar companions to the TOI-2533 system through a search leveraging both Gaia DR3 and existing adaptive optics constraints (see Appendix).

4. Joint Spin–Orbit Modeling

We used the ALLESFITTER Python package (Günther & Daylan 2021) to jointly model the new RM measurement along with other publicly available data sets for TOI-2533. The star was observed during TESS Sectors 23 and 50 at 1800 s and 600 s cadence, respectively. Sector 23 data were processed by the Science Processing Operations Center (Jenkins et al. 2016) standard aperture pipeline and retrieved using the LIGHTKURVE software package (Lightkurve Collaboration et al. 1812), while Sector 50 data were processed using the TESS Quick-Look Pipeline (Kunimoto et al. 2022) and retrieved from the Mikulski Archive for Space Telescopes (MAST).[5] Outliers in the data were removed with an upper sigma clipping of 2 away from the median.

Archival radial velocity data, obtained with the Tillinghast Reflector Échelle Spectrograph (TRES) spectrograph (Mink 2011), were drawn from Schmidt et al. (2023). To remove systematic instrumental trends characterized by a gradual increase/decrease in the measured stellar flux over time in the TESS data, we applied a detrending model following the method outlined in Ivshina & Winn (2022), where a polynomial of either first, second, or third order is selected based on a minimization of the Bayesian Information Criterion of the data.

The free parameters in our joint model include the companion-to-star radius ratio ($R_b/R_\star$), sum of radii divided by the orbital semimajor axis ($(R_\star + R_b)/a_b$), cosine of the orbital inclination ($\cos i_b$), transit epoch ($T_{0;b}$), orbital period (P_b; with initial guess as reported in Schmidt et al. 2023), radial velocity semiamplitude (K_b), orbital eccentricity and argument of periapsis coupled as $\sqrt{e}\cos(\omega)$ and $\sqrt{e}\sin(\omega)$, limb-darkening coefficients in quadratic form for TESS ($q_{1;\mathrm{TESS}}$ and $q_{2;\mathrm{TESS}}$) and NEID ($q_{1;\mathrm{NEID}}$ and $q_{2;\mathrm{NEID}}$) data (see Kipping 2013 and Espinoza & Jordán 2016 for details), jitter terms for the NEID and TRES data sets that were added in quadrature, and a white noise flux error scaling term for the TESS photometry (see Günther & Daylan 2021). The sky-projected spin–orbit angle λ was allowed to freely vary between $\pm 180°$, and the projected stellar rotation velocity $v \sin i_\star$ was also set as a free parameter. The priors for each hyperparameter are summarized in Table 2, and the host star priors were drawn from Schmidt et al. (2023)—specifically, $R_\star = 1.11 \pm 0.01\, R_\odot$, $M_\star = 1.02^{+0.06}_{-0.07}\, M_\odot$, and $T_{\mathrm{eff},\star} = 6180 \pm 60$ K.

The Markov hyperparameter space was probed using the Dynamic Nested Sampling algorithm DYNESTY (Speagle 2020) over 1000 live points and tolerance of the convergence criterion of 0.01 (see details in Günther & Daylan 2021). The resulting orbital and physical parameters derived for TOI-2533 *b* are listed in Table 2, and the RM best-fit model, along with the transit and RV models, is presented in Figure 1.

We find that the TOI-2533 b brown dwarf is consistent with spin–orbit alignment, with $\lambda = -7° \pm 14°$. This measurement is shown in context with the current census of exoplanet and brown-dwarf spin–orbit constraints in Figure 2. All other derived system parameters—corresponding to a brown dwarf with a radius $R_b = 0.841 \pm 0.018\, R_{\mathrm{Jup}}$ and mass $74.9 \pm 5.3\, M_{\mathrm{Jup}}$, on a short-period ($P = 6.685784 \pm 0.000013$ days) and moderately eccentric ($e = 0.2476 \pm 0.0090$) orbit—match with those of Schmidt et al. (2023) within 1σ.

5. Dynamical Timescales

Interactions with the primary star in a two-body system may provide a damping mechanism to push a misaligned or eccentric orbit toward its lowest energy state (e.g., Jackson et al. 2008; Matsumura et al. 2010). In this section, we examine relevant dynamical timescales and discuss their implications for the evolutionary history of TOI-2533 *b*.

5.1. Tidal Realignment and Turbulent Friction

Cross-comparing with Figure 9 from Spalding & Winn (2022), we conclude that, based on the host star's effective temperature $T_{\mathrm{eff}} = 6180 \pm 60$ K and its metallicity [Fe/H] $= -0.3 \pm 0.2$ as reported in Schmidt et al. (2023), TOI-2533 most likely hosts a convective envelope and lies below the Kraft break (Kraft 1967). We note that TOI-2533's projected stellar rotational velocity $v \sin i_* = 8.4^{+1.5}_{-1.4}$ km s^{-1} is consistent with the star lying either below or above the Kraft break (see e.g., Louden et al. 2021). Stars with convective envelopes have efficient magnetic dynamos at a young age—especially relevant for star-disk interactions over timescales of a few million years—which may facilitate orbital realignment (Spalding & Batygin 2015).

Furthermore, star-companion tidal interactions push systems toward low obliquities over time. Stars above the Kraft break possess radiative envelopes and shallower convective zones, typically resulting in longer predicted tidal realignment timescales within the equilibrium tides framework (e.g., Albrecht et al. 2012; Rice et al. 2022a). For hot Jupiters, realignment may also be induced through a coupling of the companion's orbit and the host star's oscillation modes (i.e., gravity modes in the stellar interior) that preferentially realign systems with cool stellar hosts (Zanazzi et al. 2024); however, this mechanism does not extend to systems with companion masses greater than a few Jupiter masses.

Since TOI-2533 falls within a temperature range directly coinciding with the Kraft break transition, we consider both the case in which it does and does not have a substantive convective envelope. For stars with significant convective envelopes, i.e., those below the Kraft break, the empirical tidal realignment timescale can be estimated within the equilibrium

[5] https://exo.mast.stsci.edu

Table 2
Orbital and Physical Properties Derived for TOI-2533 *b* Using `allesfitter`

Description	Parameter	Value	Prior
Fitted Parameters			
Orbital period (days)	P_b	6.685784 ± 0.000013	$\mathcal{U}(6.68577\|6.67577, 6.69577)$
Transit epoch (BJD)	$T_{0;b}$	$2459521.72862^{+0.00097}_{-0.0010}$	$\mathcal{U}(2459494\|2459466, 2459522)$
Radial velocity semiamplitude (km s^{-1})	K_b	7.579 ± 0.070	$\mathcal{U}(7\|0, 15)$
1st eccentricity parameter	$\sqrt{e_b}\cos\omega_b$	-0.104 ± 0.013	$\mathcal{U}(0\|-1, 1)$
2nd eccentricity parameter	$\sqrt{e_b}\sin\omega_b$	0.487 ± 0.010	$\mathcal{U}(0\|-1, 1)$
Companion-to-star radius ratio	$R_b/R_\star$	0.0779 ± 0.0015	$\mathcal{T}(0.075\|0.08, 0.4, 0, 1)$
Summed radii divided by semimajor axis	$(R_\star + R_b)/a_b$	0.0808 ± 0.0019	$\mathcal{T}(0.077\|0.077, 0.5, 0, 1)$
Cosine of the orbital inclination	$\cos i_b$	0.0421 ± 0.0060	$\mathcal{T}(0.0347\|0.0685, 0.0113, 0, 1)$
Sky-projected spin–orbit angle (deg)	λ	-7 ± 14	$\mathcal{U}(0\|-180, 180)$
Stellar rotation velocity (km s^{-1})	$v \sin i_*$	$8.4^{+1.5}_{-1.4}$	$\mathcal{U}(5\|1, 50)$
Quadratic limb-darkening coefficient for TESS	$q_{1;\mathrm{TESS}}$	$0.26^{+0.23}_{-0.15}$	$\mathcal{U}(0.5\|0, 1)$
Quadratic limb-darkening coefficient for TESS	$q_{2;\mathrm{TESS}}$	$0.19^{+0.30}_{-0.14}$	$\mathcal{U}(0.5\|0, 1)$
Quadratic limb-darkening coefficient for NEID	$q_{1;\mathrm{NEID}}$	$0.63^{+0.25}_{-0.32}$	$\mathcal{U}(0.5\|0, 1)$
Quadratic limb-darkening coefficient for NEID	$q_{2;\mathrm{NEID}}$	$0.60^{+0.28}_{-0.37}$	$\mathcal{U}(0.5\|0, 1)$
TESS jitter	$\ln\sigma_{\mathrm{TESS}}$	$-6.681^{+0.060}_{-0.056}$	$\mathcal{U} - 7.0\|-15, 0)$
NEID jitter (km s^{-1})	$\ln\sigma_{\mathrm{jit.;\ NEID}}$	$-10.6^{+3.3}_{-3.0}$	$\mathcal{U}(-4.5\|-15, 0)$
TRES jitter (km s^{-1})	$\ln\sigma_{\mathrm{jit.;\ TRES}}$	$-2.38^{+0.51}_{-0.67}$	$\mathcal{U}(-3.0\|-15, 0)$
Derived Brown Dwarf Parameters			
Radius, units of Earth radii ($R_\oplus$)	R_b	9.43 ± 0.20	⋯
Radius, units of Jupiter radii (R_Jup)	R_b	0.841 ± 0.018	⋯
Mass, units of Jupiter masses (M_Jup)	M_b	74.9 ± 5.3	⋯
Mass, units of solar masses ($M_\odot$)	M_b	0.0715 ± 0.0051	⋯
Mass ratio ($M_b/M_\star$)	$\equiv q_\mathrm{b}$	$0.0702^{+0.0021}_{-0.0019}$	⋯
Eccentricity	e_b	0.2476 ± 0.0090	⋯
Argument of periastron (deg)	ω_b	102.0 ± 1.6	⋯
Semimajor axis (au)	a_b	0.0688 ± 0.0017	⋯
Semimajor axis over host radius	$a_\mathrm{b}/R_\star$	13.34 ± 0.30	⋯
Inclination (deg)	i_b	87.59 ± 0.34	⋯
Impact parameter	$b_{\mathrm{tra;b}}$	0.425 ± 0.055	⋯
Total transit duration (hr)	$T_{\mathrm{tot;b}}$	$2.961^{+0.053}_{-0.049}$	⋯
Companion density (cgs)	ρ_b	156^{+16}_{-14}	⋯
Equilibrium temperature (K)	$T_{\mathrm{eq;b}}$	1095 ± 17	⋯
Transit depth (ppm)	$\delta_{\mathrm{tr;\ undil;\ b;\ TESS}}$	6740^{+210}_{-180}	⋯
Linear limb-darkening coefficient for TESS	$u_{1;\ \mathrm{TESS}}$	$0.19^{+0.21}_{-0.13}$	⋯
Linear limb-darkening coefficient for TESS	$u_{2;\ \mathrm{TESS}}$	$0.30^{+0.27}_{-0.30}$	⋯
Linear limb-darkening coefficient for NEID	$u_{1;\ \mathrm{NEID}}$	0.85 ± 0.55	⋯
Linear limb-darkening coefficient for NEID	$u_{2;\ \mathrm{NEID}}$	$-0.13^{+0.50}_{-0.43}$	⋯

Note. (a) $\mathcal{U}(\xi|\alpha, \beta)$ denotes a uniform distribution between α and β with initial guess ξ, and $\mathcal{T}(\xi|\mu, \sigma, \zeta, \eta)$ denotes a normal distribution with mean μ and standard deviation σ, truncated at lower and upper bounds (ζ, η) with initial guess ξ. (b) The transformation between quadratic to linear limb-darkening coefficients is given by $u_1 = 2\sqrt{q_1}\,q_2$ and $u_2 = \sqrt{q_1}(1 - 2q_2)$, following Kipping (2013) and Günther & Daylan (2021).

tides framework as (Albrecht et al. 2012)

$$\tau_{\mathrm{CE}} = 10^{10} q^{-2} \left(\frac{a/R_\star}{40}\right)^6, \tag{1}$$

calibrated from observations made in binary star systems by Zahn (1977). Here, $q \equiv M_\mathrm{b}/M_*$ represents the mass ratio of the companion to the host star, and $a/R_\star$ denotes the companion's orbital separation scaled by the stellar radius. Hotter stars with radiative envelopes follow a separate empirical scaling given as

$$\tau_{\mathrm{RA}} = 6.25 \times 10^9 q^{-2}(1 + q)^{-5/6} \left(\frac{a/R_\star}{6}\right)^{17/2}. \tag{2}$$

Based on our derived properties for the TOI-2533 system, we find that $\tau_{\mathrm{CE}} \sim 10^9$ yr and $\tau_{\mathrm{RA}} \sim 10^{15}$ yr. If the host star possesses a substantial convective envelope, the system's age and τ_{CE} coincide within a 3σ margin ($\Gamma = 4.26^{+2.18}_{-1.74}$ Gyr; Schmidt et al. 2023), such that the companion may have plausibly realigned over its lifetime if it formed in or was previously excited to a misaligned configuration. Alternatively, if the host star has a radiative envelope, the system would be difficult to realign within the system lifetime, implying that the observed alignment is likely primordial.

5.2. Eccentricity Evolution Driven by Tidal Dissipation

For comparison with the system's tidal realignment timescale, we also consider the evolution timescale of TOI-2533 *b*'s orbital eccentricity $\tau_e \sim e/\dot{e}$. Assuming that the brown dwarf is in pseudo-synchronous rotation—i.e., that its rotational frequency Ω is commensurate with its orbital angular frequency at periastron (although see Dewberry 2024, which describes

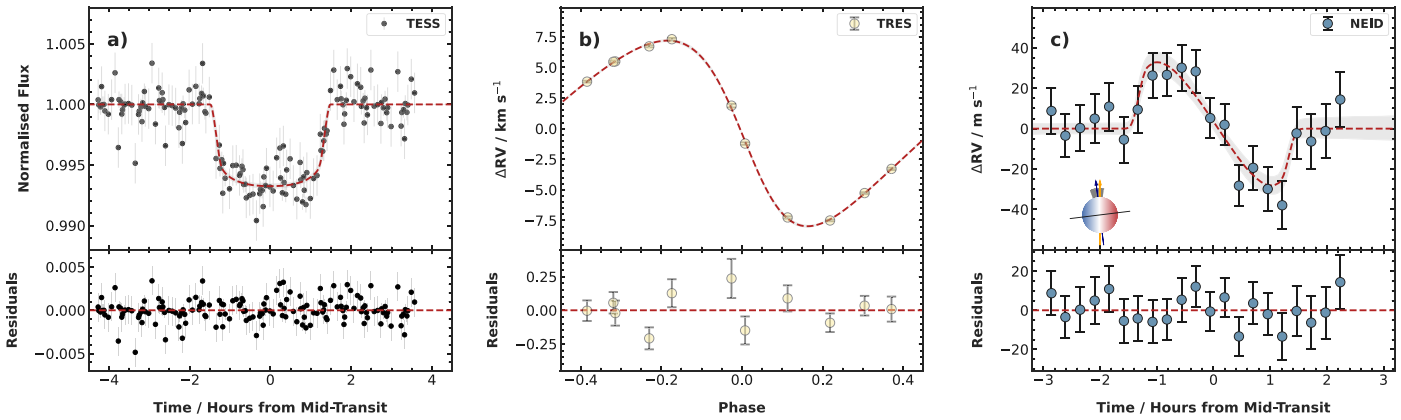


Figure 1. Best-fit joint model for TOI-2533 *b*. Panel (a) presents the phase-folded TESS light curve, panel (b) the TRES radial velocity observations, and panel (c) the NEID Rossiter–McLaughlin observations. The residuals are presented at the bottom of each panel, along with the 1σ uncertainty of the joint model in gray. A schematic representation of the TOI-2533 *b* side-view orbit is presented at the bottom left of the panel (c), corresponding to a sky-projected obliquity of $\lambda = -7^{\circ} \pm 14^{\circ}$.

possible expected deviations from pseudo-synchronization)—its energy dissipation rate can be expressed as

$$\dot{e} = \left[\frac{21 k_2 G M_*^2 \Omega R_*^5 \zeta(e)}{2\mathcal{Q} a^6}\right] \frac{a(1-e^2)}{G M_* M_b e}, \tag{3}$$

where M_* and R_* correspond to the mass and radius of the star, and M_b refers to the companion's mass. Both Ω and the corrective factor $\zeta(e)$ depend on the companion's eccentricity, with each given as (Hut 1981; Wisdom 2008)

$$\Omega = \frac{1}{P}\left[\frac{f_1(e)}{f_2(e)\beta^3}\right], \tag{4}$$

$$\zeta(e) = \frac{2}{7}\left[\frac{f_0(e)}{\beta^{15}} - 2\frac{f_1(e)}{\beta^{12}} + \frac{f_2(e)}{\beta^9}\right], \tag{5}$$

where

$$f_0(e) = 1 + \frac{31}{2}e^2 + \frac{255}{8}e^4 + \frac{185}{16}e^6 + \frac{25}{64}e^8, \tag{6}$$

$$f_1(e) = 1 + \frac{15}{2}e^2 + \frac{45}{8}e^4 + \frac{5}{16}e^6, \tag{7}$$

$$f_2(e) = 1 + 3e^2 + \frac{3}{8}e^4, \text{ and,} \tag{8}$$

$$\beta \equiv \sqrt{1-e^2}. \tag{9}$$

Following Rice et al. (2022a), we set fiducial values $\mathcal{Q} = 10^5$ as the companion's effective tidal dissipation parameter and $k_2 = 0.3$ as the Love number, which represents the companion's rigidity and susceptibility of its shape to change in response to a tidal potential.

For TOI-2533 *b*, we estimate $\tau_e \sim 10^{12}$ yr, which exceeds the proper system's age by three orders of magnitude. Therefore, we anticipate that, if TOI-2533 has a substantive convective envelope, the system should tidally realign before its orbital circularization.

6. Discussion

6.1. Comparison of TOI-2533 b with Theoretical Models for Brown Dwarfs

Fully convective objects with Kelvin–Helmholtz timescales on the order of a few million years were postulated around sixty years ago by Kumar (1963a, 1963b), and despite the discovery of over 4000 brown dwarfs so far,[6] ongoing debate continues to refine our understanding of their formation mechanisms within the context of star and planet formation. Such objects fall short of initiating hydrogen nuclear fusion, with upper masses spanning $M \sim M_{\rm HBMM} = 0.07 - 0.09\,M_{\odot}$ (Burrows et al. 2001; Forbes & Loeb 2019; Chabrier et al. 2023), but are massive enough for deuterium burning in their cores ($M > M_{\rm DBMM} = 11$–$16.3\,M_{\rm Jup}$; Spiegel et al. 2011). Relatively high-mass brown dwarfs ($\gtrapprox 60\ M_{\rm Jup}$) have radii predominantly regulated by electron-degeneracy pressure, while those at the lower limit ($\sim$15–20 $M_{\rm Jup}$) are mainly constrained by Coulomb pressure (Basri & Brown 2006).

The mass of TOI-2533 *b* ($M_b = 74.9 \pm 5.3\,M_{\rm Jup} = 0.0715 \pm 0.0051\,M_{\odot}$) falls marginally within the hydrogen-burning minimum mass regime (0.07–0.09 $M_{\odot}$), leaving its classification ambiguous between a brown dwarf and an ultracool dwarf star (see Figure 3). Notably, TOI-2533 *b*'s mass falls above the lithium-burning minimum mass limit ($M_{\rm LBMM} \sim 51.4\,M_{\rm Jup}$ Martín et al. 2022). Nevertheless, lithium absorption features are not expected in the brown dwarf's spectrum, since lithium is expected to be completely depleted in brown-dwarf atmospheres older than 100–250 Myr (e.g., Basri 2000; Kirkpatrick et al. 2008).

Evolutionary models for field brown dwarfs suggest that objects with ages around 0.5 Gyr exhibit radii comparable to those of Jovian planets, while high-mass brown dwarfs ($\geqslant 50\,M_{\rm Jup}$) tend to shrink over time, resulting in radii smaller than $1\,R_{\rm Jup}$ after 1 Gyr (Baraffe et al. 2003; Burrows et al. 2011; Chabrier et al. 2023). This contrasts with the straightforward mass-based pattern observed in stars ($R \propto M^{\xi}$, with $\xi \in \mathbb{R}^+$; Kippenhahn et al. 2013). The estimated radius of TOI-2533 *b* is $0.841 \pm 0.018\,R_{\rm Jup}$ based on our TESS light curve modeling (see Section 4), consistent with theoretical predictions given the object's mass ($M_b = 74.9 \pm 5.3\,M_{\rm Jup}$) and age ($4.26^{+2.18}_{-1.74}$ Gyr; see Figure 3).

6.2. Possible Formation Scenarios for TOI-2533 b

At first glance, TOI-2533 *b* appears similar to a scaled-up hot-Jupiter system, with a very short orbital period

[6] As of 2024 February; see the UltracoolSheet v2.0.0 catalog (Best et al. 2024).

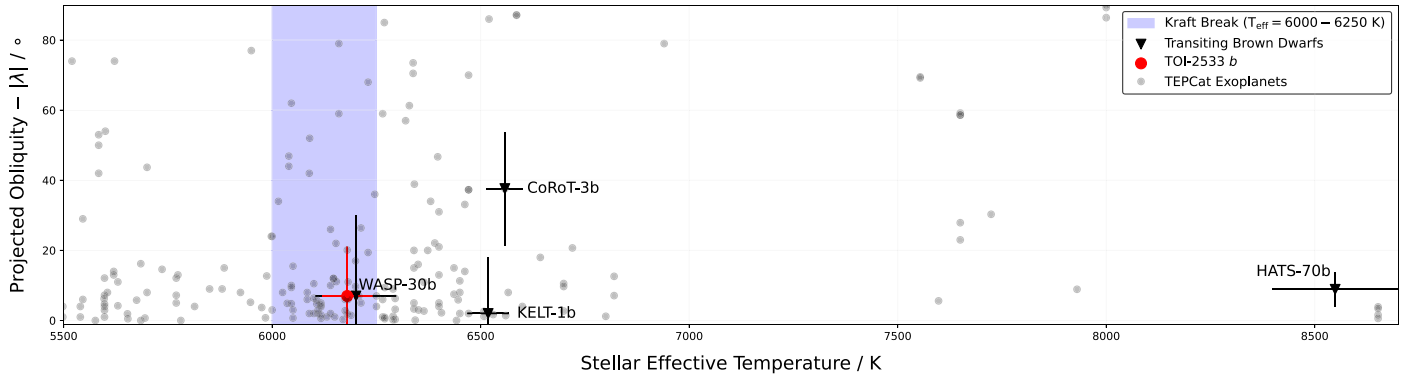


Figure 2. Distribution of the sky-projected spin–orbit angle $|\lambda|$ as a function of the stellar effective temperature for brown dwarfs and exoplanets. TOI-2533 *b*, reported in this paper, is indicated in red. Background gray dots represent exoplanets presented in the TEPCat catalog (Southworth 2011) as of 2024 May, and black triangles indicate the four known transiting brown dwarfs with previously reported spin–orbit measurements (WASP-30 *b*, CoRoT-3 *b*, KELT-1 *b*, and HATS-70 *b*). The shaded blue area represents the approximate limits of the Kraft break, for which the precise location is a function of the stellar metallicity (Spalding & Winn 2022).

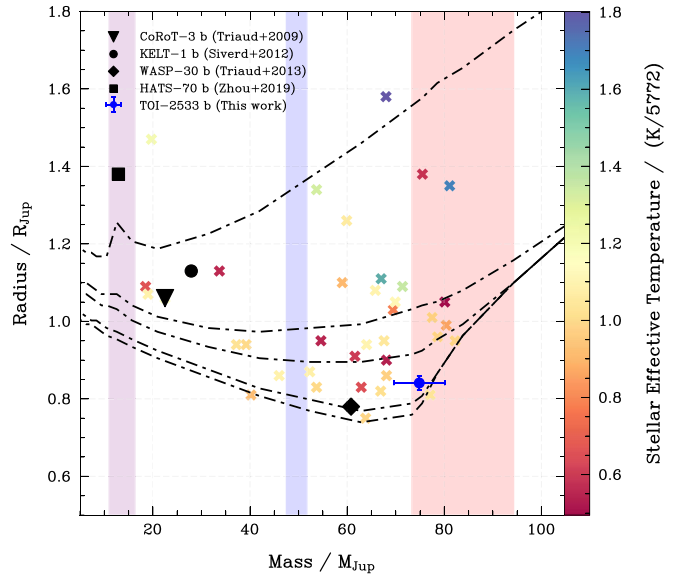


Figure 3. Mass–radius diagram for the sample of known transiting brown dwarfs as of 2023 September (Carmichael 2023). The known transiting brown dwarfs to date with measured spin–orbit angles are indicated as black symbols. COND isochrones with ages 0.1, 0.5, 1, 5, and 10 Gyr, neglecting dust opacity in the radiative transfer equation, are indicated as dashed lines (top to bottom; Baraffe et al. 2003). For reference, the age of the TOI-2533 system (indicated as a blue dot) is estimated as $4.26^{+2.18}_{-1.74}$ Gyr (Schmidt et al. 2023). Colors indicate the stellar effective temperature scaled by the Sun's ($T_{\rm eff} = 5772$ K), and the shaded regions (left to right) show the boundaries for the deuterium-burning minimum mass (purple), lithium-burning minimum mass (blue), and hydrogen-burning minimum mass (pink).

($P \sim 6.68$ days) but higher mass ($M \sim 75\,M_{\rm Jup}$). Short-period brown dwarfs around Sun-like stars also have a very low projected occurrence rate ($\lesssim$2%) comparable to the ~1% occurrence rate of hot Jupiters (Kiefer et al. 2019; Offner et al. 2023). While the brown dwarf's aligned and moderately eccentric orbit may be suggestive of mechanisms such as coplanar high-eccentricity migration (Petrovich 2015), no outer planetary companion is known to date, and the brown dwarf's eccentricity evolution is slow compared to the system's age (see Section 5). Therefore, formation through high-eccentricity migration, as has been suggested for hot Jupiters based on their stellar obliquity distribution (Rice et al. 2022a), is unlikely for this system.

The high mass of TOI-2533 *b*, together with the system's relatively high mass ratio (see Table 2), instead suggests a formation process reminiscent of stellar binary systems (Duchêne & Kraus 2013). Several mechanisms have been proposed to explain the formation of close binary systems, including gravitational capture (e.g., Fabian et al. 1975; Kaplan et al. 2012), turbulent fragmentation (e.g., Offner et al. 2010; Kratter 2011), and disk fragmentation (e.g., Hoyle 1953; Bonnell & Bate 1994).

Gravitational capture, in which a companion is captured into a bound orbit by the gravitational well of the primary star, typically occurs in dense environments (e.g., Fabian et al. 1975; Clarke & Pringle 1991; Binney & Tremaine 2008; Kaplan et al. 2012, and references therein). In globular clusters, the capture rate of brown dwarfs by main-sequence stars has been estimated with an upper limit of 15% based on the absence of observed transits in the 47 Tucanæ globular cluster (Gilliland et al. 2000; Bonnell et al. 2003), whereas the capture rate should be lower for brown dwarfs born in loose stellar clusters with a comparatively low number density (Gaudi 2003). Thus, while somewhat rare, gravitational capture may be consistent with the low occurrence rate of short-period brown dwarfs around Sun-like stars ($\lesssim$2%; Kiefer et al. 2019; Offner et al. 2023) and remains as a possibility for the formation of TOI-2533 *b*.

In the framework of turbulent fragmentation, density perturbations within a molecular core already under collapse induce fragmentation into smaller cores or filaments when their Jeans mass is exceeded, leading to the formation of gravitationally bound binary or multiple body systems (Padoan & Nordlund 2002; Goodwin et al. 2004; Offner et al. 2010, 2023; Kuffmeier et al. 2019). Turbulent fragmentation is typically expected to produce no preferential directionality of spin–orbit orientations due to the stochasticity of angular momenta throughout the molecular cloud. As a result, turbulent fragmentation would naturally produce an isotropic distribution of primordial spin–orbit orientations (Offner et al. 2010; Lee et al. 2017). Since TOI-2533 most likely has a convective envelope, and, in that case, the system has a relatively short tidal realignment timescale $\tau_{\rm CE}$, it is possible that the system may have formed through turbulent fragmentation and subsequently realigned to its currently observed orbital configuration.

Disk fragmentation during the second collapse phase of a molecular cloud[7] is a third potential pathway to form close stellar binaries (Tsuribe & Inutsuka 1999; Whitworth & Stamatellos 2006; Perets & Kratter 2012; Tokovinin & Moe 2020). In this scenario, a rotating molecular cloud flattens into a disk-like structure before its fragmentation (see Figure 1 in Bodenheimer et al. 1980, and Krumholz et al. 2009; Bate 2011), which takes place when there is a sufficiently high ratio between rotational and gravitational energies during the freefall collapse phase (Wurster et al. 2018). These fragments break into smaller ones, increasing density, opacity, and temperature until further fragmentation ceases (Prialnik 2009). Accretion of material onto these proto-brown dwarfs continues until their surrounding gas dissipates and before they reach stellar masses (Bate et al. 2002; Umbreit 2005). Disk fragmentation naturally produces aligned and moderately eccentric close-in systems like TOI-2533 *b* (Bonnell & Bate 1994; Hale 1994; Laughlin & Bodenheimer 1994; Kratter et al. 2010), with no need to invoke tidal realignment.

While the formation mechanism for TOI-2533 *b* remains ambiguous across these three mechanisms, the system highlights the need for further brown-dwarf spin–orbit constraints. In particular, brown dwarfs with long projected tidal realignment timescales may inform how the broader population of short-period brown dwarfs, including TOI-2533 *b*, likely reached their tight orbits. An extended sample of brown-dwarf spin–orbit orientations has the potential to more generally inform the dynamical pathways that sculpt main-sequence/brown-dwarf binaries.

7. Conclusions

TOI-2533 *b* stands out as the fifth transiting brown dwarf with a measured spin–orbit angle reported to date, as well as the twelfth result of the SOLES survey. We have leveraged in-transit radial velocity observations from the NEID/WIYN spectrograph to show that TOI-2533 *b*'s orbit is consistent with alignment, with a low-sky-projected spin–orbit angle, $\lambda = -7^\circ \pm 14^\circ$, that falls within the range observed for quiescent near-resonant exoplanet systems (Rice et al. 2023b) —a possible tracer of primordial circumstellar disk alignments.

With its aligned and moderately eccentric orbit, TOI-2533 *b*'s origin is consistent with stellar binary-like formation through disc fragmentation. This formation pathway is consistent with the brown dwarf's relatively high mass $M_b = 74.9 \pm 5.3\, M_{\rm Jup}$ and relatively high-mass ratio $q = 0.0702^{+0.0021}_{-0.0019}$. However, we cannot rule out the possibility that the system initially had a larger misalignment that was corrected over its lifetime, given the short tidal realignment timescale $\tau_{\rm CE}$ in the case that the host star has a significant convective envelope. Further brown-dwarf spin–orbit measurements across a wider parameter space, particularly for systems with long projected tidal realignment timescales, would offer useful insights to delineate the range of orbital architectures for these intermediate-mass eclipsing systems.

[7] In the first collapse phase, also known as the isothermal phase, the number density around the center of the cloud is on the order of $n_c \leqslant 10^{11}$ cm^{-3}, while the second collapse occurs when $n_c > 10^{16}$ cm^{-3} and the cloud reaches a temperature of about 2000 K, causing molecular H_2 dissociation and a reduction of the adiabatic constant $\gamma \equiv C_P/C_V$ to $\gamma_{\rm critical} < 4/3$ (Larson 1969).

Acknowledgments

T.F. acknowledges support from Yale Graduate School of Arts and Sciences. M.R. acknowledges support from Heising-Simons Foundation grant #2023-4478, Oracle for Research grant No. CPQ-3033929, and JPL/NASA grant #1709150. S. W. acknowledges support from the Heising-Simons Foundation grant #2023-4050. We acknowledge support from the NASA Exoplanets Research Program NNH23ZDA001N-XRP (grant No. 80NSSC24K0153). This paper contains data taken with the NEID instrument, which was funded by the NASA-NSF Exoplanet Observational Research (NN-EXPLORE) partnership and built by Pennsylvania State University. NEID is installed on the WIYN telescope, which is operated by the National Optical Astronomy Observatory, and the NEID archive is operated by the NASA Exoplanet Science Institute at the California Institute of Technology. NN-EXPLORE is managed by the Jet Propulsion Laboratory, California Institute of Technology under contract with the National Aeronautics and Space Administration. All TESS data used in this paper can be downloaded from MAST:10.17909/vpkg-8e10.

Facilities: FLWO:1.5m:NEID, TESS, FLWO:1.5m:TRES.

Software: `numpy` (Harris et al. 2020), `pandas` (The pandas development team 2023), `astropy` (Astropy Collaboration et al. 2013, 2018, 2022), `matplotlib` (Hunter 2007), `smplotlib` (Li 2023), `lightkurve` (Lightkurve Collaboration et al. 1812), , `allesfitter` (Günther & Daylan 2021), `dynesty` (Speagle 2020), `tpfplotter` (Aller et al. 2020), `VOSA` (Bayo et al. 2008).

Appendix
No Bound Stellar Companions to TOI-2533

An inspection of the TESS Target Pixel Files (TPF) using the TPFPLOTTER[8] (Aller et al. 2020) software initially revealed two nearby sources with $\Delta G \leqslant 6$ mag relative to TOI-2533: (i) Gaia DR3 1259922127931777664 ($\mu_\alpha = -1.62 \pm 0.02$ mas yr^{-1}, $\mu_\delta = 2.91 \pm 0.02$ mas yr^{-1}, $\overline{\pi} = 0.025 \pm 0.023$ mas) and (ii) Gaia DR3 1259921754269906560 ($\mu_\alpha = -12.50 \pm 0.02$ mas yr^{-1}, $\mu_\delta = 15.62 \pm 0.01$ mas yr^{-1}, $\overline{\pi} = 1.71 \pm 0.02$ mas).

The 3D velocity difference between Gaia DR3 125992175 4269906560 and TOI-2533 is $\Delta v_{\rm 3D} \sim 13.77$ km s^{-1} based on the two stars' parallax and proper motion measurements, surpassing the threshold of $\Delta v_{\rm 3D} \leqslant 2$ km s^{-1} typically associated with gravitationally bound objects with $a < 10^7$ au (Kamdar et al. 2019). Gaia DR3 1259921754269906560 maintains a projected separation of 53.″07 from TOI-2533, corresponding to approximately 19,600 au. While the projected angular separation between TOI-2533 and Gaia DR3 1259922127931777664 is smaller, at 42.″05, the projected distance between the two stars is much larger, at $d \sim 38{,}910 \pm 35{,}579$ pc from inverting the parallax of Gaia DR3 (although we caution that this approach overestimates large distances; see, e.g., Herpich et al. 2021). By employing corrections from Bailer-Jones et al. (2021), the median geometric distance is found to be $d \sim 11{,}422^{+2613}_{-1762}$ pc. Therefore, the likelihood that either star is gravitationally bound to TOI-2533 is low.

Neither of these two sources nor TOI-2533 itself is present in the catalog of binary systems presented by El-Badry et al. (2021). We also note that no close-separation companions have been identified within a ∼8″ field of view from high-resolution

[8] https://github.com/jlillo/tpfplotter

adaptive optics imaging on the Exoplanet Follow-up Observing Program (ExoFOP) website.[9]

ORCID iDs

Thiago Ferreira dos Santos https://orcid.org/0000-0003-2059-470X
Malena Rice https://orcid.org/0000-0002-7670-670X
Xian-Yu Wang https://orcid.org/0000-0002-0376-6365
Songhu Wang https://orcid.org/0000-0002-7846-6981

References

Albrecht, S., Setiawan, J., Torres, G., Fabrycky, D. C., & Winn, J. N. 2013, ApJ, 767, 32
Albrecht, S., Winn, J. N., Johnson, J. A., et al. 2012, ApJ, 757, 18
Albrecht, S. H., Dawson, R. I., & Winn, J. N. 2022, PASP, 134, 082001
Aller, A., Lillo-Box, J., Jones, D., Miranda, L. F., & Barceló Forteza, S. 2020, A&A, 635, A128
Astropy Collaboration, Price-Whelan, A. M., Lim, P. L., et al. 2022, ApJ, 935, 167
Astropy Collaboration, Price-Whelan, A. M., Sipőcz, B. M., et al. 2018, AJ, 156, 123
Astropy Collaboration, Robitaille, T. P., Tollerud, E. J., et al. 2013, A&A, 558, A33
Bailer-Jones, C. A. L., Rybizki, J., Fouesneau, M., Demleitner, M., & Andrae, R. 2021, AJ, 161, 147
Baraffe, I., Chabrier, G., Barman, T. S., Allard, F., & Hauschildt, P. H. 2003, A&A, 402, 701
Basri, G. 2000, ARA&A, 38, 485
Basri, G., & Brown, M. E. 2006, AREPS, 34, 193
Bate, M. R. 2011, MNRAS, 417, 2036
Bate, M. R., Bonnell, I. A., & Bromm, V. 2002, MNRAS, 332, L65
Bate, M. R., Bonnell, I. A., & Bromm, V. 2003, MNRAS, 339, 577
Bate, M. R., Lodato, G., & Pringle, J. E. 2010, MNRAS, 401, 1505
Bayo, A., Rodrigo, C., Barrado Y Navascués, D., et al. 2008, A&A, 492, 277
Benitez, N., Dupke, R., Moles, M., et al. 2014, arXiv:1403.5237
Best, W. M. J., Dupuy, T. J., Liu, M. C., et al. 2024, The UltracoolSheet: Photometry, Astrometry, Spectroscopy, and Multiplicity for 4000+ Ultracool Dwarfs and Imaged Exoplanets, v2.0.0, Zenodo, doi:10.5281/ZENODO.4169084
Binney, J., & Tremaine, S. 2008, Galactic Dynamics: Second Edition (Princeton, NJ: Princeton Univ. Press)
Blanco-Cuaresma, S. 2019, MNRAS, 486, 2075
Blanco-Cuaresma, S., Soubiran, C., Heiter, U., & Jofré, P. 2014, A&A, 569, A111
Bodenheimer, P., Tohline, J. E., & Black, D. C. 1980, ApJ, 242, 209
Bonnell, I. A., & Bate, M. R. 1994, MNRAS, 271, 999
Bonnell, I. A., Clark, P., & Bate, M. R. 2008, MNRAS, 389, 1556
Bonnell, I. A., Clarke, C. J., Bate, M. R., et al. 2003, MNRAS, 343, L53
Boss, A. P. 1997, Sci, 276, 1836
Bowler, B. P., Blunt, S. C., & Nielsen, E. L. 2020, AJ, 159, 63
Burrows, A., Heng, K., & Nampaisarn, T. 2011, ApJ, 736, 47
Burrows, A., Hubbard, W. B., Lunine, J. I., & Liebert, J. 2001, RvMP, 73, 719
Carmichael, T. W. 2023, MNRAS, 519, 5177
Carmichael, T. W., Irwin, J. M., Murgas, F., et al. 2022, MNRAS, 514, 4944
Carmichael, T. W., Quinn, S. N., Zhou, G., et al. 2021, AJ, 161, 97
Cenarro, A. J., Moles, M., Cristóbal-Hornillos, D., et al. 2019, A&A, 622, A176
Chabrier, G., Baraffe, I., Phillips, M., & Debras, F. 2023, A&A, 671, A119
Clarke, C. J., & Pringle, J. E. 1991, MNRAS, 249, 584
Dewberry, J. W. 2024, ApJ, 966, 180
Dong, J., Wang, S., Rice, M., et al. 2023, ApJL, 951, L29
Duchêne, G., & Kraus, A. 2013, ARA&A, 51, 269
El-Badry, K., Rix, H.-W., & Heintz, T. M. 2021, MNRAS, 506, 2269
Espinoza, N., & Jordán, A. 2016, MNRAS, 457, 3573
Fabian, A. C., Pringle, J. E., & Rees, M. J. 1975, MNRAS, 172, 15
Forbes, J. C., & Loeb, A. 2019, ApJ, 871, 227
Gaia Collaboration, Vallenari, A., Brown, A. G. A., et al. 2023, A&A, 674, A1
Gaudi, B. S. 2003, arXiv:astro-ph/0307280
Gilliland, R. L., Brown, T. M., Guhathakurta, P., et al. 2000, ApJL, 545, L47
Goodwin, S. P., & Whitworth, A. 2007, A&A, 466, 943
Goodwin, S. P., Whitworth, A. P., & Ward-Thompson, D. 2004, A&A, 414, 633
Günther, M. N., & Daylan, T. 2021, ApJS, 254, 13
Hale, A. 1994, AJ, 107, 306
Harris, C. R., Millman, K. J., van der Walt, S. J., et al. 2020, Natur, 585, 357
Herpich, F. R., Ferreira Lopes, C. E., Saito, R. K., et al. 2021, A&A, 647, A169
Hixenbaugh, K., Wang, X.-Y., Rice, M., & Wang, S. 2023, ApJL, 949, L35
Høg, E., Fabricius, C., Makarov, V. V., et al. 2000, A&A, 357, 367
Holt, J. R. 1893, AstAp, 12, 646
Hoyle, F. 1953, ApJ, 118, 513
Hu, Q., Rice, M., Wang, X.-Y., et al. 2024, AJ, 167, 175
Huber, D., Stello, D., Bedding, T. R., et al. 2009, CoAst, 160, 74
Hunter, J. D. 2007, CSE, 9, 90
Hut, P. 1981, A&A, 99, 126
Ivshina, E. S., & Winn, J. N. 2022, ApJS, 259, 62
Jackson, B., Greenberg, R., & Barnes, R. 2008, ApJ, 678, 1396
Jenkins, J. M., Twicken, J. D., McCauliff, S., et al. 2016, Proc. SPIE, 9913, 99133E
Kamdar, H., Conroy, C., Ting, Y.-S., et al. 2019, ApJ, 884, 173
Kaplan, K. F., Bender, C. F., Terrien, R. C., et al. 2019, in ASP Conf. Ser. 523, Astronomical Data Analysis Software and Systems XXVII, ed. P. J. Teuben et al. (San Francisco, CA: ASP), 567
Kaplan, M., Stamatellos, D., & Whitworth, A. P. 2012, Ap&SS, 341, 395
Kesseli, A. Y., West, A. A., Veyette, M., et al. 2017, ApJS, 230, 16
Kiefer, F., Hébrard, G., Sahlmann, J., et al. 2019, A&A, 631, A125
Kippenhahn, R., Weigert, A., & Weiss, A. 2013, Stellar Structure and Evolution (Berlin: Springer)
Kipping, D. M. 2013, MNRAS, 435, 2152
Kirkpatrick, J. D., Cruz, K. L., Barman, T. S., et al. 2008, ApJ, 689, 1295
Kraft, R. P. 1967, ApJ, 150, 551
Kratter, K. M. 2011, in ASP Conf. Ser. 447, Evolution of Compact Binaries, ed. L. Schmidtobreick, M. R. Schreiber, & C. Tappert (San Francisco, CA: ASP), 47
Kratter, K. M., Matzner, C. D., Krumholz, M. R., & Klein, R. I. 2010, ApJ, 708, 1585
Krumholz, M. R., Klein, R. I., McKee, C. F., Offner, S. S. R., & Cunningham, A. J. 2009, Sci, 323, 754
Kuffmeier, M., Calcutt, H., & Kristensen, L. E. 2019, A&A, 628, A112
Kumar, S. S. 1963a, ApJ, 137, 1121
Kumar, S. S. 1963b, ApJ, 137, 1126
Kunimoto, M., Tey, E., Fong, W., et al. 2022, RNAAS, 6, 236
Larson, R. B. 1969, MNRAS, 145, 271
Laughlin, G., & Bodenheimer, P. 1994, ApJ, 436, 335
Lee, J.-E., Lee, S., Dunham, M. M., et al. 2017, NatAs, 1, 0172
Li, J. 2023, AstroJacobLi/smplotlib: v0.0.9, Zenodo, doi:10.5281/zenodo.8126529
Lightkurve Collaboration, Cardoso, J. V. d., Hedges, C., et al., 1812 Lightkurve: Kepler and TESS Time Series Analysis in Python, Astrophysics Source Code Library, ascl:1812.013
Louden, E. M., Winn, J. N., Petigura, E. A., et al. 2021, AJ, 161, 68
Lubin, J., Wang, X.-Y., Rice, M., et al. 2023, ApJL, 959, L5
Ma, B., & Ge, J. 2014, MNRAS, 439, 2781
Maldonado, J., & Villaver, E. 2017, A&A, 602, A38
Martín, E. L., Lodieu, N., & del Burgo, C. 2022, MNRAS, 510, 2841
Matsumura, S., Peale, S. J., & Rasio, F. A. 2010, ApJ, 725, 1995
McLaughlin, D. B. 1924, ApJ, 60, 22
Mink, D. J. 2011, in ASP Conf. Ser. 442, Astronomical Data Analysis Software and Systems XX, ed. I. N. Evans et al. (San Francisco, CA: ASP), 305
Naoz, S., Farr, W. M., Lithwick, Y., Rasio, F. A., & Teyssandier, J. 2011, Natur, 473, 187
Naoz, S., Farr, W. M., & Rasio, F. A. 2012, ApJL, 754, L36
Offner, S. S. R., Dunham, M. M., Lee, K. I., Arce, H. G., & Fielding, D. B. 2016, ApJL, 827, L11
Offner, S. S. R., Kratter, K. M., Matzner, C. D., Krumholz, M. R., & Klein, R. I. 2010, ApJ, 725, 1485
Offner, S. S. R., Moe, M., Kratter, K. M., et al. 2023, in ASP Conf. Ser. 534, Protostars and Planets VII, ed. S. Inutsuka et al. (San Francisco, CA: ASP), 275
Padoan, P., & Nordlund, Å. 2002, ApJ, 576, 870
Perets, H. B., & Kratter, K. M. 2012, ApJ, 760, 99
Petrovich, C. 2015, ApJ, 805, 75
Prialnik, D. 2009, An Introduction to the Theory of Stellar Structure and Evolution (Cambridge: Cambridge Univ. Press)
Psaridi, A., Bouchy, F., Lendl, M., et al. 2022, A&A, 664, A94
Radzom, B. T., Dong, J., Rice, M., et al. 2024, AJ, 168, 116
Rice, M., Gerbig, K., & Vanderburg, A. 2024, AJ, 167, 126

[9] https://exofop.ipac.caltech.edu/tess/

Rice, M., Wang, S., Gerbig, K., et al. 2023a, AJ, 165, 65
Rice, M., Wang, S., Howard, A. W., et al. 2021, AJ, 162, 182
Rice, M., Wang, S., & Laughlin, G. 2022a, ApJL, 926, L17
Rice, M., Wang, S., Wang, X.-Y., et al. 2022b, AJ, 164, 104
Rice, M., Wang, X.-Y., Wang, S., et al. 2023b, AJ, 166, 266
Ricker, G. R., Winn, J. N., Vanderspek, R., et al. 2015, JATIS, 1, 014003
Rossiter, R. A. 1924, ApJ, 60, 15
Schlaufman, K. C. 2010, ApJ, 719, 602
Schlaufman, K. C. 2018, ApJ, 853, 37
Schmidt, S. P., Schlaufman, K. C., Ding, K., et al. 2023, AJ, 166, 225
Schwab, C., Rakich, A., Gong, Q., et al. 2016, Proc. SPIE, 9908, 99087H
Siverd, R. J., Beatty, T. G., Pepper, J., et al. 2012, ApJ, 761, 123
Skrutskie, M. F., Cutri, R. M., Stiening, R., et al. 2006, AJ, 131, 1163
Southworth, J. 2011, MNRAS, 417, 2166
Spalding, C., & Batygin, K. 2015, ApJ, 811, 82
Spalding, C., & Winn, J. N. 2022, ApJ, 927, 22
Speagle, J. S. 2020, MNRAS, 493, 3132
Spiegel, D. S., Burrows, A., & Milsom, J. A. 2011, ApJ, 727, 57
Šubjak, J., Sharma, R., Carmichael, T. W., et al. 2020, AJ, 159, 151
Teyssandier, J., Lai, D., & Vick, M. 2019, MNRAS, 486, 2265
The pandas development team 2023, pandas-dev/pandas: Pandas, v2.2.0rc0, Zenodo, doi:10.5281/zenodo.3509134
Tohline, J. E. 2002, ARA&A, 40, 349
Tokovinin, A., & Moe, M. 2020, MNRAS, 491, 5158
Triaud, A. H. M. J., Hebb, L., Anderson, D. R., et al. 2013, A&A, 549, A18
Triaud, A. H. M. J., Queloz, D., Bouchy, F., et al. 2009, A&A, 506, 377
Tsuribe, T., & Inutsuka, S.-i. 1999, ApJL, 523, L155
Umbreit, S. 2005, PhD thesis, Ruprecht Karl Univ. Heidelberg doi:10.11588/heidok.00005702
Viani, L. S., Basu, S., Corsaro, E., Ball, W. H., & Chaplin, W. J. 2019, ApJ, 879, 33
Wang, X.-Y., Rice, M., Wang, S., et al. 2022, ApJL, 926, L8
Whitworth, A. P., & Stamatellos, D. 2006, A&A, 458, 817
Windhorst, R. A., Cohen, S. H., Hathi, N. P., et al. 2011, ApJS, 193, 27
Winn, J. N., Fabrycky, D., Albrecht, S., & Johnson, J. A. 2010, ApJL, 718, L145
Winn, J. N., Howard, A. W., Johnson, J. A., et al. 2009, ApJ, 703, 2091
Wisdom, J. 2008, Icar, 193, 637
Wright, E. L., Eisenhardt, P. R. M., Mainzer, A. K., et al. 2010, AJ, 140, 1868
Wright, J., Rice, M., Wang, X.-Y., Hixenbaugh, K., & Wang, S. 2023, AJ, 166, 217
Wurster, J., Bate, M. R., & Price, D. J. 2018, MNRAS, 480, 4434
York, D. G., Adelman, J., Anderson, J. E. J., et al. 2000, AJ, 120, 1579
Zahn, J. P. 1977, A&A, 57, 383
Zanazzi, J. J., Dewberry, J., & Chiang, E. 2024, ApJL, 967, L29
Zechmeister, M., & Kürster, M. 2009, A&A, 496, 577
Zhou, G., Bakos, G. Á, Bayliss, D., et al. 2019, AJ, 157, 31